Path instability and wake of a rising bubble

Woodrow L. Shew, Sébastien Poncet, Jean-Francois Pinton

Path instability and wake of a rising bubble

Woodrow L. Shew, Sebastien Poncet, and Jean-François Pinton
Laboratoire de Physique, École Normale Supérieur de Lyon
Lyon, France 69007

The dynamics of millimeter sized air bubbles rising through still water are investigated using precise ultrasound velocity measurements combined with high speed video. From measurements we deduce the forces acting on the bubble and we tie the dynamics of the bubble's wake to observed oscillatory instabilities of the bubble's path: planar zigzag and spiraling motion.

I. BACKGROUND

As a bubble ascends from the bottom of a body of water, it induces motion in the fluid. The buoyant forces which drive the bubble's rise do work resulting in an increase in kinetic energy of the surrounding fluid. This induced flow, in turn, causes changes in the path of the bubble. These nonlinear interactions between a bubble and the fluid motion it induces are the subject of the work presented here.

An understanding of bubble-fluid interactions, in general, is important in a broad range of natural, engineering, and medical settings. Air-sea gas transfer, bubble column reactors, oil/natural gas transport, boiling heat transfer, ship hydrodynamics, ink-jet printing and medical ultrasound imaging are just a few examples where the dynamics of bubbles play a role (e.g [6, 16, 26]).

We narrow our focus to a single air bubble rising through still water. Our study includes a range of bubble sizes between 0.84 and 1.2 mm in radius. At the small end of this range the bubble path is rectilinear and its wake is steady and axisymmetric. As the bubble size is increased, one observes the generation of a double-threaded vortex wake and the transition to a planar zigzag path [8, 23]. A second instability, often preceded by the zigzag, results in a spiraling path, which is also accompanied by the double-threaded wake vortices [5, 8, 15, 23]. Fo even larger bubbles, a third type of oscillating path occurs, which looks similar to the zigzag, sometimes called "rocking". We do not address this state and emphasize that it is different than the zigzag mentioned above. Unlike the zigzag state that we study, the rocking bubble undergoes dramatic shape oscillations, periodically discharges turbulent bursts into its wake, and oscillates at frequencies several times higher than the zigzag or spiral [5, 15, 29]. The goal of our work is to better understand the physical mechanisms which relate the onset and saturation of zigzag and spiral path instabilities to the structure and time evolution of the bubble's wake.

The dynamics of bubble path instabilities have puzzled researchers for quite a long time. Leonardo Davinci is likely the first scientist to have contributed to the significant body of work addressing this problem [26]. Clift et al. [6] review relevant studies prior to about 1978. In 2002, Magnaudet and Eames [16] provided a thorough account of more recent work on this subject. Our attention will be limited to those works which address bubble path instabilities. Saffman in 1956 [27], Hartunian and Sears in 1957 [11], and later Benjamin in 1984 [4] attempted to explain features of the path instabilities and bubble shape by analytical means, but experiments are not in accord with their findings. Several experimental works have visualized and documented the shape of zigzagging and spiraling bubble paths without attempting to explain causal mechanisms [1, 2, 17, 30]. Other recent studies have investigated path instabilities with special attention paid to the role of the bubble's wake. We will only briefly describe these works now, referring to more details later in the text when appropriate. The understanding of bubble wake structure that we invoke in the discussions to follow is derived from our own quantitative measurements of bubble paths in conjunction with the findings of these studies. Lunde and Perkins used dye to observe the wake of ascending bubbles and solid particles [15]. Brücker used particle image velocimetry to study the wake of large spiraling and rocking bubbles [5]. Mougin and Magnaudet presented numerical observations of the path and wake of a bubble with a rigid ellipsoidal shape [23]. de Vries et al. used Schlieren optics techniques to visualize the wakes of zigzagging and spiraling bubbles [8]. Finally, Ellingsen and Risso used laser doppler anenometry and cameras to measure the path as well as the flow around the bubble [10].

Some of these studies have focused on the role of vorticity production and transport in the dynamics of path instabilities [15, 23]. They argue qualitatively that, for larger bubbles, vorticity production is too large to be transported away from the bubble in an axisymmetric wake. As a result, the wake develops a non-axisymmetric form which more efficiently transports vorticity and also gives rise to path instability. We approach the problem from a complementary and more quantitative point of view. We experimentally measure the trajectories of bubbles with unprecedented precision in velocity over large rise distances. We use our measurements to estimate the forces acting on the bubble and develop an explanation of path instabilities in terms of the path geometry and structure of the wake.

In the next section we describe the experimental apparatus and measurement techniques, as well a typical bubble trajectory. In section III, we present a method for extracting force measurements from path and velocity measurements based on the generalized Kirchhoff equations. Then, in section IV, we discuss some observations of the

bubble trajectory during the first few hundred milliseconds after release. We describe the zigzagging instability in section V and the spiral motion in section VI. Finally we conclude and discuss some remaining open questions concerning our data and bubble path instabilities.

II. EXPERIMENTAL APPARATUS AND METHODS

One goal of this work is to obtain measurements of bubble behavior rising through a large distance, revealing the long time dynamics of the zigzag and spiral instabilities. To this effect, the experiments are conducted in a tank 2 m in height and 30 cm wide with square cross section as illustrated in Fig. 1. The walls are made of 1.45 cm thick acrylic plate. Bubbles are produced at the bottom of the vessel by pumping air through a 24 gauge stainless steel capillary tube with a 0.30 mm inner diameter (ID) and a 0.56 mm outer diameter (OD). The tube is oriented with its open end facing upwards. The air is pumped to the capillary tube through a length of Tygon tubing (0.51 mm ID and 2.3 mm OD, from Cole-Parmer) using a peristaltic pump (Roto-Consulta, flocon 1003). The rotor of the pump is turned by hand, releasing a single bubble. We always allow at least 3 minutes delay between the release of consecutive bubbles to be sure that the water is truly quiescent for each bubble.

The volume of each bubble is measured individually. When the bubble reaches the top of the vessel it is trapped under a submerged plate. Using a syringe, each bubble is sucked into a transparent section of Tygon tubing (ID 0.51 ± 0.005 mm) with water on either side of the bubble. The length of the air plug in the tube is then measured with calipers (± 0.2 mm precision). Knowing the tube inner diameter one then calculates the bubble volume. In the results that follow, an equivalent radius $R \equiv (3/4\pi \times \text{actual volume})^{1/3}$ is used as a measure of the bubble size. During the ascent, R increases by 6% due to the gradient in hydrostatic pressure. This expansion is accounted for in the calculations of forces. Furthermore, each instance where the bubble radius or Reynolds number is presented in this paper it is properly adjusted for the pressure at the height of the bubble being described. The Reynolds number is defined $Re = 2RU/\nu$, where U is the current speed of the bubble and ν is the kinematic viscosity of water. We have observed speeds in the range $32 < U < 36$ cm/s, yielding Reynolds numbers $500 < Re < 770$.

Some of our force calculations depend on the shape of the bubble. It has been shown by other experimenters that the bubble is close to an oblate ellipsoid [8, 9, 10, 29]. Since we do not make such measurements, we use the experimental results of Duineveld [9] to estimate the shape of our bubbles. Wu and Gharib [30] measured aspect ratios which confirm Duineveld's results. The aspect ratio of the bubbles in our size range is well approximated by a linear function of bubble equivalent radius. The aspect ratio χ is defined as the length of the semimajor axis divided by the length of the semiminor axis. In fig. 2, we show Duineveld's results and the linear fit,

$$\chi(R) = 2.18R - 0.10. \quad (1)$$

This method of estimating χ is justified by the agreement of our measurements with Moore's drag theory [18] as shown below in Fig. 8 in section IV.

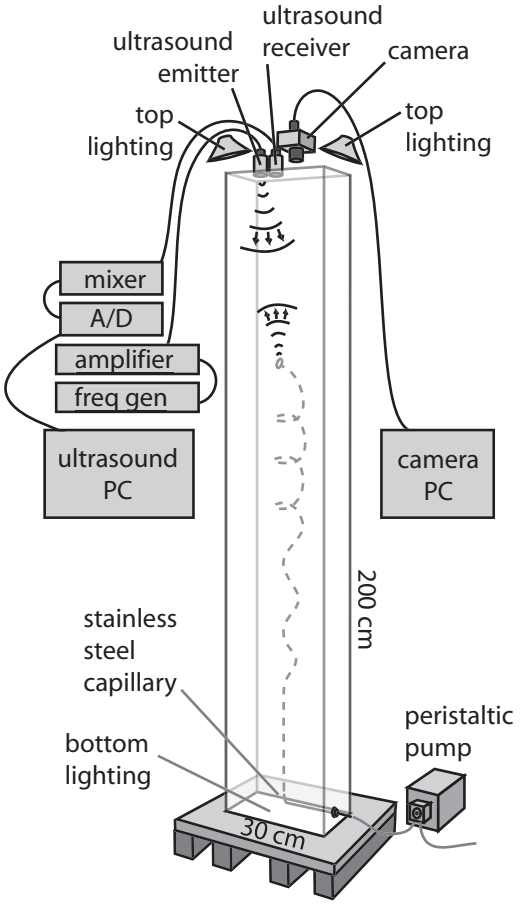

FIG. 1: Schematic of experimental setup. As the bubble rises its vertical velocity is measured using ultrasound and its horizontal position is obtained with a high speed video camera.

Before each experiment the vessel and all parts exposed to the water are thoroughly cleaned with methanol, dried, and then rinsed with tap water for 5 minutes. All data is collected with tap water less than 8 hours old. It is known that small bubbles rise more slowly in tap water compared to highly purified water due to contamination of the air-water interface with surfactants (e.g. [6, 9]). Nonetheless, several observations suggest that surfactant effects are not greatly influencing the dynamics of our bubbles, probably because of their larger size. First, our velocity measurements are consistent with Moore's drag theory and Duineveld's measurements in clean water (see fig. 8 in section IV). Second, we observe that during the straight rise of a bubble of radius 1.0 mm (at 1 atm), the velocity grows by about 2% over 1.5 m. This result is con-

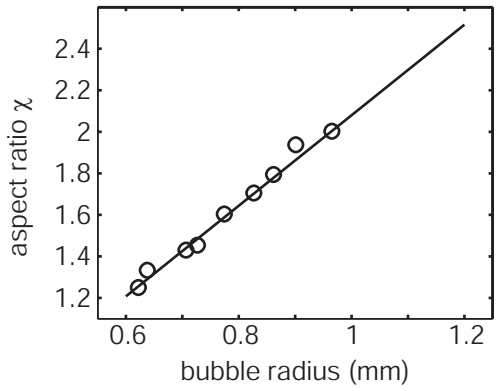

FIG. 2: Comparison of Duineveld's measurements of aspect ratio [9] and the linear model we use to estimate χ.

sistent with the increase in buoyancy and drag due the expansion of size as well as aspect ratio during ascent. If surfactant effects were significant, the bubble would slow down as it rises. We note that for bubbles smaller than about 0.75 mm in radius, our measured rise velocities reveal such a decrease in speed and are decreased compared to those of Duineveld. This indicates that, in our tap water, smaller bubbles are strongly influenced by surfactants, while large bubbles are not. The data presented in this paper is limited to bubbles larger than 0.87 mm.

Temperature is monitored at two different depths for each experiment. The mean temperature is 18.5±0.25 °C and the temperature gradient is always less than 0.009 °C/cm.

The trajectory of the bubble is measured using two methods: ultrasound and high speed video. The vertical component of the bubble velocity is obtained with high precision using a continuous ultrasound technique. We briefly describe this technique here, but for more detail the reader is referred to the references: [19, 20, 21]. One piezo-electric ultrasound transducer positioned at the top of the vessel generates a continuous 2.8 MHz sound wave directed towards the bottom. The emitted waveform is created by a Hewlett Packard arbitrary function generator (HP E1445A) and amplified by a Kalmus Engineering Model 150C 47 dB radio frequency power amp. The sound is scattered by the rising bubble and measured by an array of eight piezo ultrasound transducers (custom by Vermon), also located at the top of the vessel. Each signal measured by the eight receiving transducers is then mixed into a different frequency band, amplified, and summed using an in-house custom made circuit. After this stage, 130 dB of dynamical range is preserved. The eight channels are mixed down to one channel so that only one analog to digital converter is needed to digitize the data. The digitization is accomplished with a Hewlett Packard 10 MHz, 23 bit A/D converter (HP E1430A). All of the HP devices are VXI modules in a Hewlett Packard mainframe (HP E1421A) which interfaces with a personal computer using a fire-wire module (HP E8491A).

Once digitized, Matlab routines are used to extract the original eight channels of ultrasound data. The signal from each channel is dominated by the emitted frequency (2.8 MHz) and a lower amplitude Doppler shifted frequency of the sound scattered from the bubble. Each signal is shifted in frequency so that the emitted frequency becomes DC and hence the Doppler shifted frequency is directly proportional to the bubble velocity. In order to obtain velocity as a function of time the frequency is extracted using a numerical approximated maximum likelihood scheme coupled with a generalized Kalman filter [19].

The ultrasound method measures the component of the bubble's velocity along the line between the bubble and the ultrasound receiver. In order to obtain the true vertical component, some correction of the data is required as the bubble comes closer to the ultrasound transducer. An iterative corrective algorithm is employed beginning with the average vertical velocity and the position data from the camera data as a first estimate of the trajectory. Geometrical corrections are then made on the original velocity data based on this approximate trajectory. This new corrected velocity is then used to recompute the trajectory. The process is then iterated until convergence is reached.

The absolute accuracy of our velocity measurements was verified using a video camera. We released an object slightly heavier than water and recorded its descent with the ultrasound device and simultaneously with a camera positioned 2.5 meters away with a side view of the tank. The test showed that the ultrasound velocity measurements are consistent within 2% of the camera data. We measure top speeds of our bubbles typically about 36 cm/s, which is consistent with other experimental measurements [2, 9, 30]. The relative accuracy of our velocity measurements is more precise, typically ±1 mm/s, or about 0.2% accuracy. Furthermore, the sampling frequency is several kHz. Over a distance of 2 meters, this level of accuracy is not possible with cameras or other optical methods. Another advantage is that the ultrasound technique is potentially useful in opaque fluids.

The vertical velocity measurements provide direct observations of the kinetic energy delivered to the fluid as the bubble rises. The only energy source in the system is the work done by the buoyancy force $\mathbf{F}_b$. The power delivered to the fluid is then $\mathbf{F}_b \cdot \mathbf{U} = \rho V g U_z$, where $\rho = \rho_f - \rho_g$ is the density difference between the fluid and the gas, V is the volume of the bubble, g is acceleration due to gravity, and U_z is the vertical component of velocity of the bubble. Note that $\rho_g \ll \rho_f$, so $\rho \approx \rho_f$. In the remainder of this paper we will continue to neglect the density of the gas. For typical bubbles in our study, $U_z \approx 0.35$ m/s and the buoyancy force is $\rho V g \approx 50$ μN. Therefore the bubble produces about 10 μW of power in the form of fluid kinetic energy as it rises.

A high speed video camera (Photron Fast Cam Ultima

1024) is used to obtain the horizontal motion of the bubble. The camera is positioned above the vessel close to the ultrasound receiving array so that it records the horizontal motion of the bubble. The camera is operated at 125 frames/sec with 512 × 512 pixel resolution. The bubble is between 10 and 100 pixels wide as it rises from a depth of two meters. Lighting is provided by two incandescent lamps (125 and 100 Watts) positioned above the vessel and one (100 Watts) beneath the translucent floor. Note that most of the time series displayed later in this paper contain 125 samples/sec since they are at least partially derived from the camera data. This gives an effective time resolution of 8 ms. Time series with higher sampling rates (see section IV) are derived only from the ultrasound data, which yields a time resolution of less than 1 ms. The period of motion for typical path oscillations is around 200 ms.

The bubble position is extracted from movies using another Matlab routine. The routine subtracts frame i from frame $i+1$, then averages over a 5×5 pixel moving window and locates the maximum of the resulting image. This process is repeated, reversing the subtraction (frame i minus frame $i+1$). The position of the maxima of the two subtraction/averageing processes are then averaged and taken as the bubble position. This method is found to reliably locate the bubble center even when the camera focus and light reflected from the bubble changes during its ascent. The accuracy of the position measurements is about 3% or ± 0.1 mm. The horizontal position data is differentiated to obtain the horizontal velocity with about 6% or ±6 mm/s precision.

Trajectories were recorded for over 20 bubbles. From the vertical speed and horizontal position data we may reconstruct the entire three dimensional trajectory for each bubble as demonstrated in Fig. 3. The bubble in Fig. 3 is 1.12 mm in radius at atmospheric pressure. This example clearly demonstrates the three different types of behavior exhibited by the bubbles in the size range of our investigation. Just after the bubble is generated it accelerates quickly to its terminal speed. It rises for a short time in a nearly straight path. For a large enough bubble, the rectilinear rise soon becomes unstable to a zigzag motion. These oscillations are confined to a vertical plane (y-z plane in Fig. 3). The path then evolves into a spiral. A smooth transition occurs from zigzag to elliptical spiral, and finally to a circular spiral. This transition is shown in Fig. 4, where the trajectory is projected onto a horizontal plane.

III. FORCES ON BUBBLES

The equations of motion for a rigid body moving through a fluid at rest were established in the context of potential flow theory more than a century ago by Kirchhoff (for an English translation see [13]). Like in other analytical approaches to understanding bubble dynamics, potential flow theory describes the gross features, but regions of the flow with vorticity must be accounted for to make precise predictions. Kirchhoff's equations have been generalized to the case of viscous, rotational flow [12] and, more recently, used in numerical work [22, 23] to investigate the behavior of freely rising bubbles with a fixed shape. The numerical work revealed the same zigzagging and spiraling paths as we and others have observed experimentally as well as quantitative agreement with path oscillation amplitudes and frequencies. These results strongly suggest that shape changes to the bubble do not play a critical role in the dynamics. Based on this result and experimental observations of steady bubble shapes for the bubble sizes we study [7, 10], we assume that bubble shape is fixed and therefor we may use the generalized Kirchhoff equations. The equations govern the six degrees of freedom necessary to completely specify the angular velocity $\mathbf{\Omega}$ and the linear velocity $\mathbf{U}$ of the body. Using the notation of [22, 23], we have

$$\mathbb{D}\frac{\mathrm{d}\mathbf{\Omega}}{\mathrm{d}t} = \mathbf{\Gamma} - \mathbf{\Omega} \times \mathbb{D}\mathbf{\Omega} - \mathbf{U} \times \mathbb{A}\mathbf{U}, \tag{2}$$

$$\mathbb{A}\frac{\mathrm{d}\mathbf{U}}{\mathrm{d}t} = \mathbf{F} - \mathbf{\Omega} \times \mathbb{A}\mathbf{U}. \tag{3}$$

Here the velocity and angular velocity of the body is evaluated in an inertial reference frame (like our experimental measurements) and then projected onto a coordinate system which has a fixed origin and rotates with the bubble, such that the added mass tensor $\mathbb{A}$ and the added rotational inertia tensor $\mathbb{D}$ are always diagonal. $\mathbf{F}$ and $\mathbf{\Gamma}$ are respectively the net forces and torques on the bubble due to non-zero viscosity, the presence of vorticity in the flow, as well as buoyancy.

The rotating coordinate system mentioned above is precisely defined as follows. The 1-direction is always parallel to the velocity vector of the bubble. The 2-direction is at a right angle to the 1-direction and defined such that the 1-2 plane contains both the velocity and the buoyancy force vector. Finally the 3-direction is orthogonal to the 1 and 2-directions and, hence, is always purely horizontal. This coordinate system is illustrated in Fig. 5.

For a straight rising bubble, obviously $\Omega = 0$. For zigzagging and spiraling bubbles, it is has been observed in experiments and numerics that the short axis of the ellipsoidal bubble is always aligned with the bubble velocity vector [8, 10, 23]. With this knowledge, Ω is determined by the pitch angle θ and frequency f of oscillatory motions of the bubble trajectory. From geometrical considerations one may determine,

$$\mathbf{\Omega} = \begin{cases} \dot{\theta}\ \hat{\mathbf{3}}, & \text{for zigzag} \\ 2\pi f(\cos\theta\ \hat{\mathbf{1}} + \sin\theta\ \hat{\mathbf{2}}), & \text{for spiral.} \end{cases} \tag{4}$$

Combining equations 2, 3, and 4 one obtains for the zigzag,

$$\rho V C_{I3}\ddot{\theta} \ = \ \Gamma_{d3} + \Gamma_{w3}, \tag{5}$$

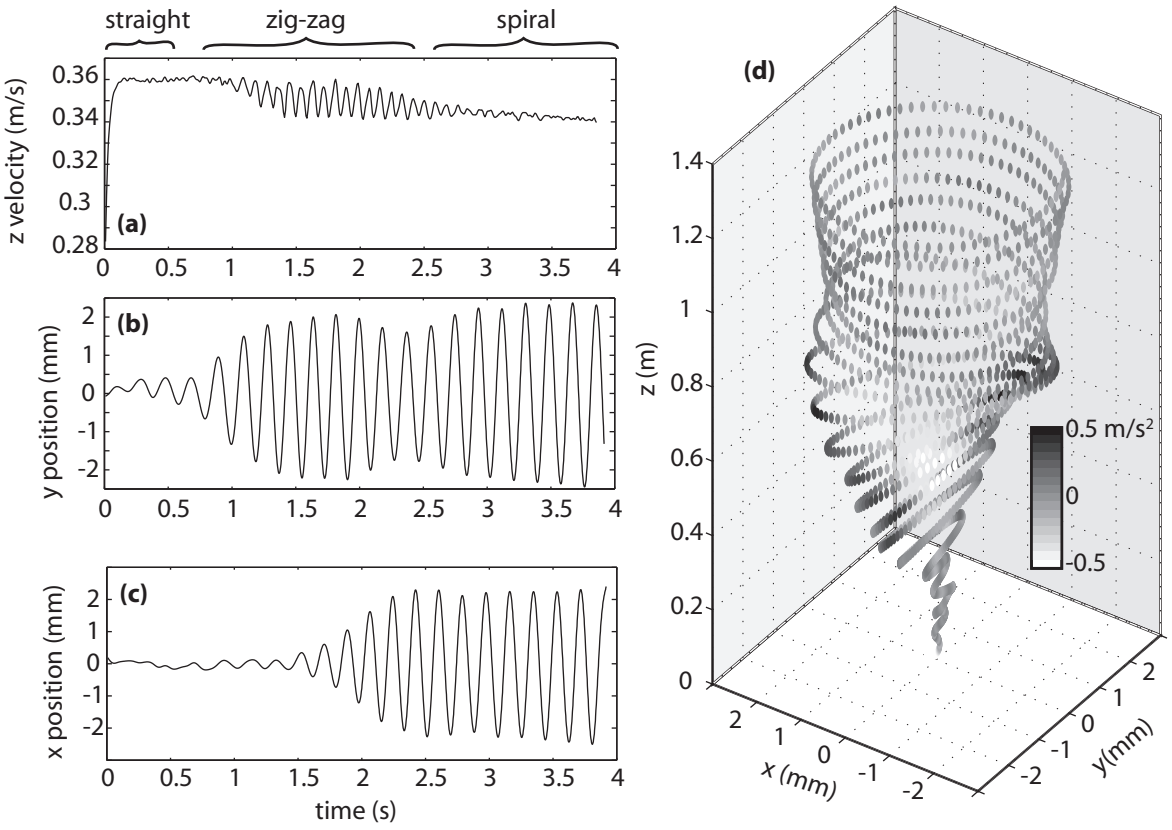

FIG. 3: Example trajectory of a 1.12 mm radius bubble (at 1 atm). (a) Vertical component of velocity as measured with ultrasound technique, (b) y position from camera data, (c) x position from camera data, and (d) three dimensional reconstruction of full trajectory with grayscale indicating magnitude of acceleration. The bubble begins rising straight, followed by zigzag motion in the (y, z) plane with oscillating velcocity, followed by a three-dimensional spiral motion with steady velocity.

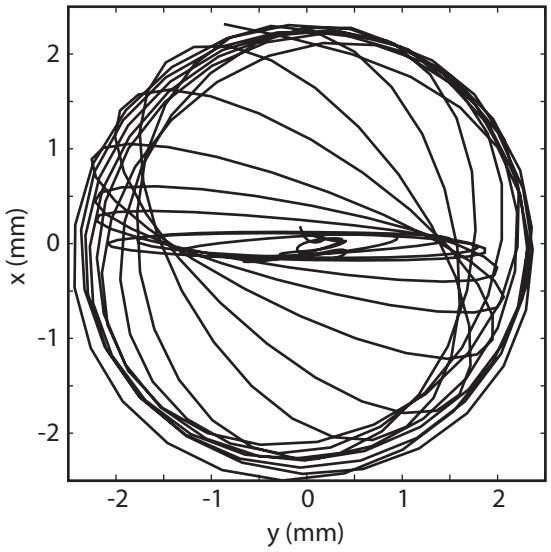

FIG. 4: Projection of a bubble trajectory onto a horizontal plane during the transition from zigzag to spiral. The bubble radius is 1.12 mm at 1 atm. The time step between plotted points is 8 ms.

$$\rho V C_{M1} a_1 = F_{b1} + F_d, \quad (6)$$

$$\rho V (C_{M2} a_2 + C_{M1} \dot{\theta} U) = F_{b2} + F_{L2} \quad (7)$$

$$(8)$$

and for the spiral,

$$0 = \Gamma_{d1} + \Gamma_{w1}, \quad (9)$$

$$0 = \Gamma_{d2} + \Gamma_{w2}, \quad (10)$$

$$0 = F_{b1} + F_d, \quad (11)$$

$$0 = F_{b2} + F_{L2} \quad (12)$$

$$\rho V (C_{M3} a_3 + C_{M1} 2\pi f \sin\theta) U = F_{L3}. \quad (13)$$

Here a_i are the components of acceleration and C_{Mi} are the added mass coefficients, which depend only on the aspect ratio of the bubble [13]. We have introduced the contributions to the net force $\mathbf{F} = \mathbf{F}_b + \mathbf{F}_d + \mathbf{F}_L$, including buoyancy, drag, and lift respectively. The buoyancy is simply $\mathbf{F}_b = \rho V \mathbf{g}$. The buoyancy generally has components in the 1 and 2 directions in proportions determined by the pitch angle. The drag always acts opposite the velocity in direction and is given by $F_d = 0.5 C_D \pi R^2 \rho U^2$, where C_D is the drag coefficient. Finally, the lift force $\mathbf{F}_L$ is perpendicular to the bubble path and causes the path curvature and balances part of the buoyancy force.

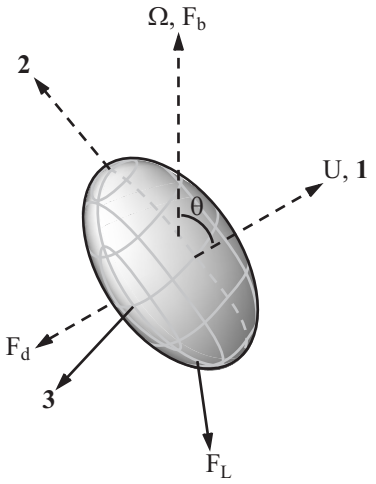

FIG. 5: Diagram of the coordinate system, velocity U, angular velocity Ω, pitch angle θ, and external forces (F_b, F_d, F_L) present for a spiraling bubble. The dashed lines line in the 1-2 plane.

Time series of the two components of lift during the trajectory shown in Fig. 3 are shown in Fig. 6. We remind the reader that for the calculation of all of these forces we account for the increasing volume and aspect ratio χ caused by the hydrostatic pressure gradient. The torques $\mathbf{\Gamma} = \mathbf{\Gamma}_d + \mathbf{\Gamma}_w$ are less well understood. $\mathbf{\Gamma}_d$ is the drag torque due to rotation and $\mathbf{\Gamma}_w$ is the wake induce torque which drives rotation. To our knowledge, no analytical predictions exist for $\mathbf{\Gamma}_d$ or $\mathbf{\Gamma}_w$.

For the rectilinear portion of bubble trajectories, Moore's theory [18] for the drag coefficient $C_D(\chi)$ matches experimental measurements. Note, however, that Moore's prediction of $\chi(R)$ does not agree with experiments and therefor one must obtain the aspect ratio from measurements. Moore's result is

$$C_D = \frac{48}{Re}G(\chi) + \frac{48}{Re^{3/2}}G(\chi)H(\chi). \qquad (14)$$

The first term on the right, $48G(\chi)/Re$ results from computing the dissipation in the flow field predicted by potential flow theory for an ellipsoid with a free-slip boundary. The second term on the right refines the calculation accounting for the rotational flow in thin boundary layers and a long thin wake. For zigzagging and spiraling bubbles, the wake becomes unstable and Moore's C_D is no longer expected to be accurate for several reasons. First, the rotational regions in the wake change drastically when the wake goes unstable and loses axisymmetry. Second, the first term on the right in equation 14 is based on the irrotational flow around a translating body and a different result is expected for a body with some rotation and unsteady speed. For the spiral this difference may be small since the speed is steady and the time scale of rotation (path oscillation period) is about 100 times the time scale for translation, $D/U \approx 3$ ms.

IV. RECTILINEAR RISE AND ONSET OF PATH INSTABILITY

Let us discuss several observations of the initial moments of the bubble's ascent up to the point where the trajectory becomes unstable. First, we observe an exponential approach to terminal speed. Second, our measurements of terminal speed agree with Moore's theory [18]. Third, as bubble size is increased the bifurcation to path instability is rather abrupt and possibly subcritical.

As shown in Fig. 7 the bubble accelerates to a terminal velocity U_o within the first 200 ms of the rise. The inset in Fig. 7 shows the velocity U subtracted from the terminal velocity U_o and plotted on a logarithmic scale. After about 20 ms, the rise is well approximated by an exponential approach to the terminal velocity. The dashed line in the inset of Fig. 7 is the equation,

$$U = U_o(1 - \mathrm{e}^{-t/\tau}), \qquad (15)$$

where the time constant $\tau = 25$ ms. We interpret τ as the approximate time required for the flow around the bubble to respond to a sudden change in the bubble's speed.

Once the bubble has attained terminal velocity it typically rises for a short period in a straight trajectory before beginning to zigzag. During this constant speed, rectilinear portion of the ascent our velocity measurements are in agreement with Moore's theory [18]. In Fig. 8, we compare our measurements of the drag coefficient C_D as a function of bubble Reynolds number to Moore's prediction (equation 14). Our measurement of C_D, depends only on the bubble size and velocity. Moore's prediction depends on the bubble size, velocity, and aspect ratio.

We observe that the height above the release point at which a bubble's path becomes unstable varies significantly with bubble size. Small bubbles can rise straight for nearly 2 meters before becoming unstable, while larger bubbles may become unstable even before reaching terminal velocity. For those bubbles whose path becomes unstable some time after reaching terminal velocity, we determine the critical radius at the onset of oscillations is 0.97 mm. Using the approximation in eqn. 1, this corresponds to a critical aspect ratio of 2.02. As a measure of the character of the bifurcation from straight to oscillating path, the average horizontal component of velocity between a height of 1.4 and 1.6 meters is shown for a range of bubble sizes in Fig. 9. The transition is rather abrupt as bubble size is increased, which suggests the bifurcation is not supercritical (see comparison to $\sqrt{R - R_{crit}}$ in Fig. 9). Mougin and Magnaudet also suggest that the onset of zigzag motions may be subcritical for increasing aspect ratio.

V. ZIGZAG INSTABILITY

It is known from previous experimental and numerical work that the onset of the zigzag instability is simultane-

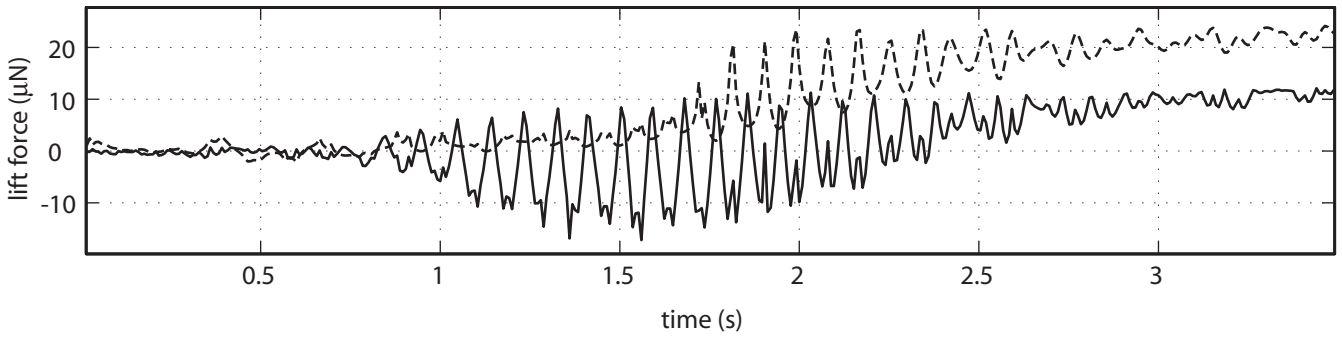

FIG. 6: The two components of lift (F_{L3}-dotted line, F_{L2}- solid line) and as measured during the trajectory shown in Fig. 3. The bubble radius is 1.12 mm at 1 atm. The measurement uncertainty is about ± 4 μN.

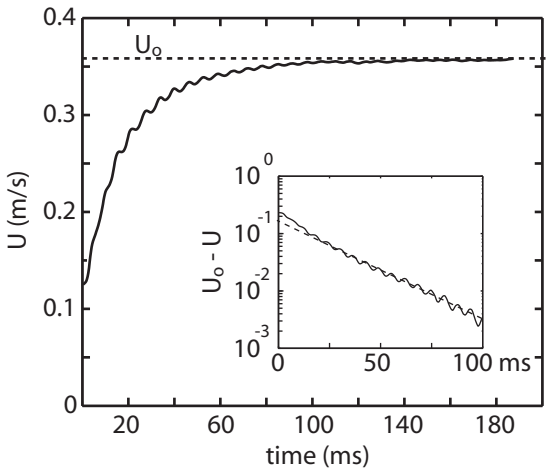

FIG. 7: Velocity during the initial 200 ms of a bubble's rise. The inset demonstrates the exponential approach to the terminal speed with a time constant of 25 ms. The bubble radius is 1.09 mm at 1 atm.

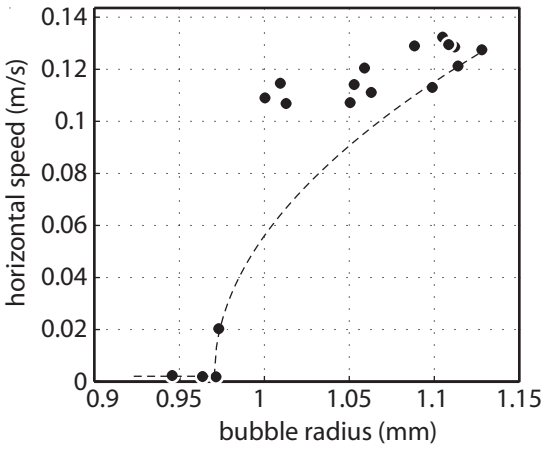

FIG. 9: Horizontal speed of bubble averaged through the interval 1.4 - 1.6 meters above release point. A supercritical bifurcation would correspond to a $\sqrt{R - R_{crit}}$ behavior (dashed line).

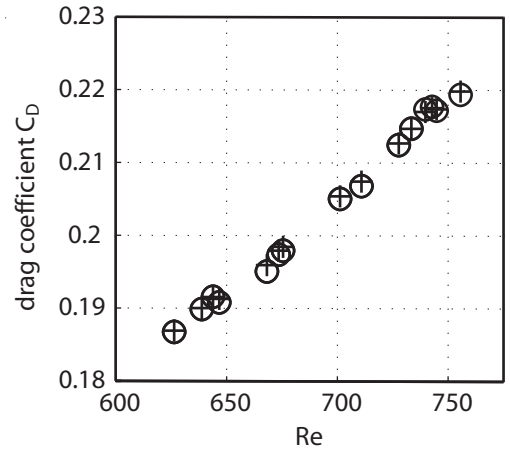

FIG. 8: Comparison of our drag coefficient measurements (circles) during the rectilinear part of the bubble trajectories to predictions of Moore's theory (+).

ous with a dramatic change in the bubble's wake. In this section, we first review what is know about the structure of the wake behind a bubble with an unstable path. Then we use this information in conjunction with our experimental measurements to explain the dynamics of the zigzag trajectory.

A. Wake structure

The wake structure of millimeter sized bubbles has been demonstrated clearly by several flow visualization experiments over the last decade [5, 8, 10, 15]. de Vries et al. were kind enough to allow us to reprint some of their Schlieren images, which we display in Fig. 10. One observes the existence of two long, thin wake vortices with opposite sense of rotation aligned with the bubble's path. For a spiraling bubble the wake vortices are continuously generated, while they are interrupted twice per period of path oscillation for the zigzag. Mougin and Magnaudet [23, 24] obtained a nearly identical wake structure in nu-

merical simulations.

The mechanism responsible for producing this wake may be similar to that which creates lift and trailing vortices on an airplane wing. This analogy was also suggested by Lunde and Perkins [15]. A wing experiences lift because the flow over its top surface is faster than the flow under its bottom surface, resulting in a lower pressure above than below (e.g. [3]). Consistently, this lift force is the time rate of increase in downward momentum imparted to the air as the wing passes. This downward momentum manifests largely in the form of wing-tip vortices, which result from the flow from high (below the wing) to low (above the wing) pressure near the ends of the wing as illustrated in Fig. 11a. A combination of the downward pumping between the vortices and an overall downward drift of the vortex system behind the wing gives rise to downward momentum transport in the fluid. By analogy, we suggest that similar velocity and pressure fields give rise to the two trailing vortices in the wake of a bubble. Streamline images from Mougin and Magnaudet's numerical simulations indicate this is a reasonable suggestion [24]. When the bubble's path is curving a lift force is acting towards the center of curvature, i.e. the flow around the bubble's surface is slower on the side outside the curve of the path creating a high pressure region there. The pressure difference then produces flow around the sides of the bubble resulting in a vortex pair in the wake, as illustrated in Fig. 11b. The critical role of the wake vortices in generating lift and, hence, path instability has also been suggested in many of the above mentioned studies [5, 8, 15, 23].

B. Zigzag dynamics and force measurements

Once the wake instability occurs and the path begins to curve, what causes the repeating change in direction as we observe in the zigzag? The answer to this question lies in the change in the balance of forces on the bubble as the path becomes inclined with respect to vertical. As the angle between the path and vertical grows, the component of buoyancy (F_{b1} as defined above) available to drive the bubble forward decreases and consequently the bubble slows down. At a lower speed the bubble can no longer maintain the wake production, so path curvature decreases and the wake dissipates. In a sense the wake cuts off its own power source, the buoyancy. The lift force, which holds the bubble's path at an angle against the influence of buoyancy, is caused by the wake. Therefore, as the wake dissipates the bubble's trajectory once again gradually returns to vertical. The bubble is able to pick up speed again, soon reaching the speed where the wake growth begins again. Consequently, the path begins to curve away from vertical, and the cyclic process starts again. de Vries et al. [8] have presented a similar explanation, but were mistaken about the time dynamics of lift forces.

This description of the zigzag is supported by our measurements of the forces on the bubble as it rises. Fig. 12a shows the evolution of the component of buoyancy tangential to the trajectory F_{b1}, the velocity, the horizontal position (x and y) of the bubble, and the two components of wake induced lift F_{L2} and F_{L3}. The lift force F_{L2} may be regarded as an indicator for the existence of the wake. The fact that F_{L3} is zero indicates that the zigzag motion is restricted to the 1-2 plane. One can see in Fig. 12 that as the lift grows the path veers away from vertical resulting in a decrease in F_{b1} and, hence, a decrease in the velocity. When the velocity is low enough, wake production and, hence, lift decrease. The path then returns to vertical and the bubble regains speed once again increasing wake production.

During the zigzag process the sense of rotation of the wake vortices reverses every time the wake dies and then is reborn [5, 8, 15, 23]. This reversal ensures that the lift and hence curvature of the bubble path reverses every half cycle of path oscillation. If the reversal did not occur a staircase-like motion would result rather than a zigzag. What causes the reversal of the wake? Once the bubble is moving at the critical speed for path instability, a symmetry breaking occurs and the wake becomes unstable to the streamwise vortex pair. After the bubble has slowed and the wake is dissipating, the path curves upwards again under the influence of buoyancy. This will initially cause slightly faster flow around the side of the bubble furthest from the center of the path curvature. This flow may provide the symmetry breaking perturbation needed to trigger the wake instability in a way that results in a lift force which enhances the curvature already started by buoyancy. In a similar way, wake production is triggered on the fast flow side of a solid sphere placed in a shear flow [28].

VI. SPIRAL MOTION

Let us shift our attention now to the dynamics of spiraling bubble motion. First, we present observations and force measurements. Then we give a hypothesis for the mechanism responsible for spiraling motion as well as the transition from zigzag.

A. Observations and forces

The transition to spiral motion is remarkable in several ways. First, we observe that every zigzagging path eventually becomes a spiral. The spiral may be clockwise or or counterclockwise. The transition to spiraling motion is not abrupt, generally developing gradually over several periods of motion as demonstrated above in Fig. 4. Bubbles may zigzag for as many as 15 and as few as 2 cycles before transitioning to the spiral. Furthermore, the transition does not seem to behave systematically with bubble size. The frequency of path oscillations remains unchanged compared to the zigzag. This is apparent in

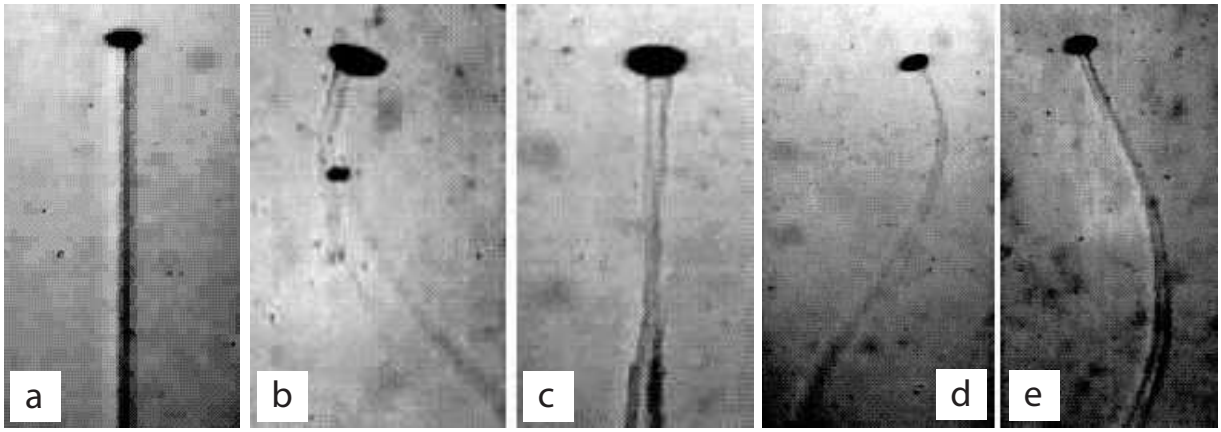

FIG. 10: Schlieren images of wake structure for (a) straight rising ($R = 0.79$ mm), (b-c) zigzagging ($R = 1.00$ mm), (d-e) and spiraling ($R = 1.01$ mm) bubbles reprinted with permission from the PhD thesis of de Vries [7]. The two photos in (b-c) show the same bubble viewed from orthogonal viewpoints. The same is true of (d-e)

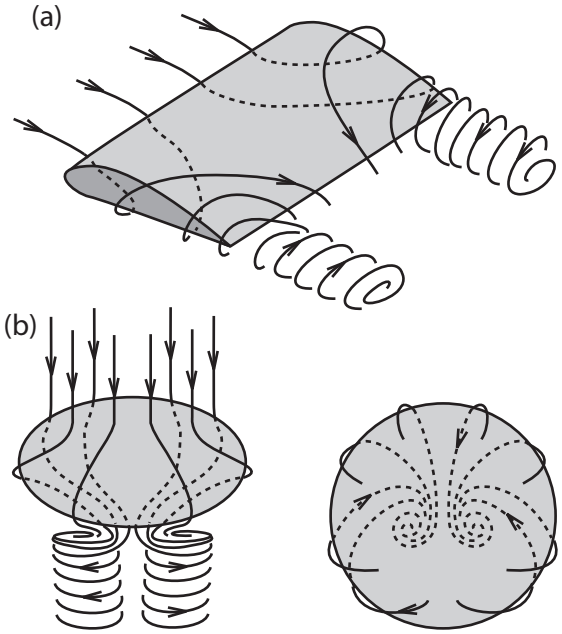

FIG. 11: (a) Flow around a wing which gives rise to trailing vortices and lift. (b) Depiction of possible flow and wake around a bubble. The dotted lines represent flow behind the object.

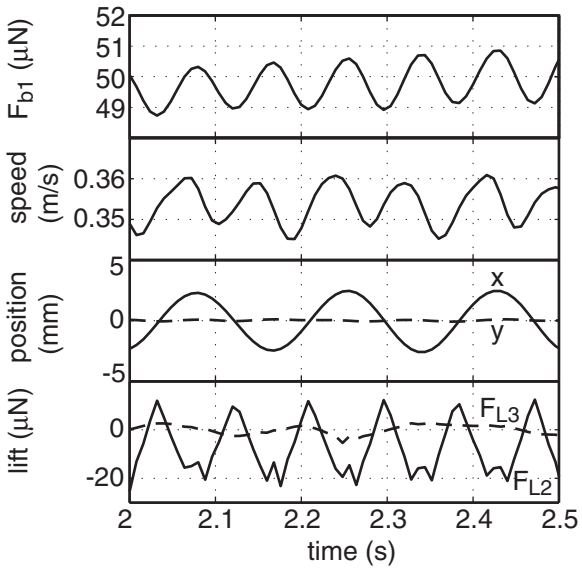

FIG. 12: The buoyancy component tangential to the path F_b1, bubble velocity, horizontal position (x and y), and (d) lift force (solid line: F_{L2} and dashed line: F_{L3}) as measured during a zigzagging trajectory. The bubble radius is 1.12 mm at 1 atm. The measurement uncertainties are ± 0.5 μN for F_{b1}, ± 7 mm/s for speed, $\pm$ 0.2 mm for position, and ± 4 μN for lift forces.

the horizontal position data shown previously in Fig. 3. The frequency increases as bubble size is increased as shown in Fig. 13.

The most striking change when the bubble stops zigzagging and begins to spiral is that all the forces and the bubble speed become steady. This is consistent with observations that the wake generation is continuous for a spiraling bubble [5, 8, 15, 29]. Fig. 14 shows time series of several features of a spiralling bubble. The top frame presents the component of buoyancy F_{b1} compared to the drag F_{dp} predicted by assuming $C_D = 48G(\chi)/Re$ as discussed in section III. Since the speed of the bubble is constant during the spiral, F_{b1} is equal to the total drag on the bubble. We observe that F_{dp} predicts the total drag within 1%. The component of wake induced lift F_{L3} is typically about twice as large as F_{L2}. This is apparent in Fig. 14 and is demonstrated for a range of bubble sizes in Fig. 15.

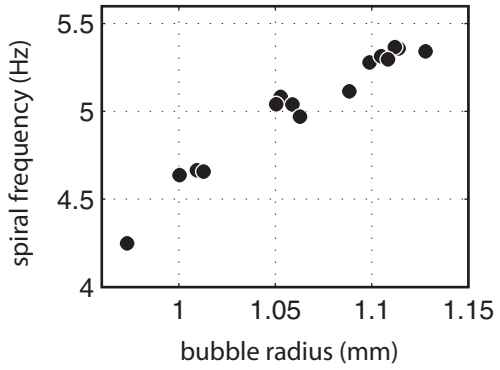

FIG. 13: The frequency of spiraling motion for a range of bubble sizes. The measurement is precise to within 2%.

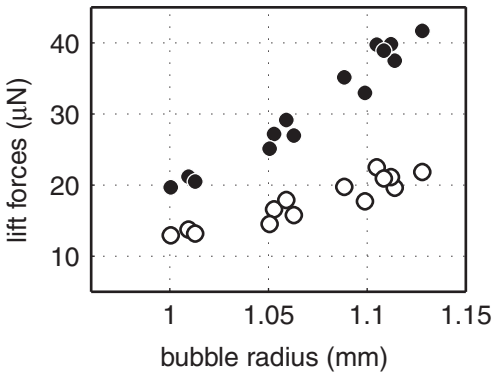

FIG. 15: Comparison of F_{L2} (open circles) and F_{L3} (solid circles) for spiraling bubbles of various sizes. The measurement uncertainty is ± 2 μN.

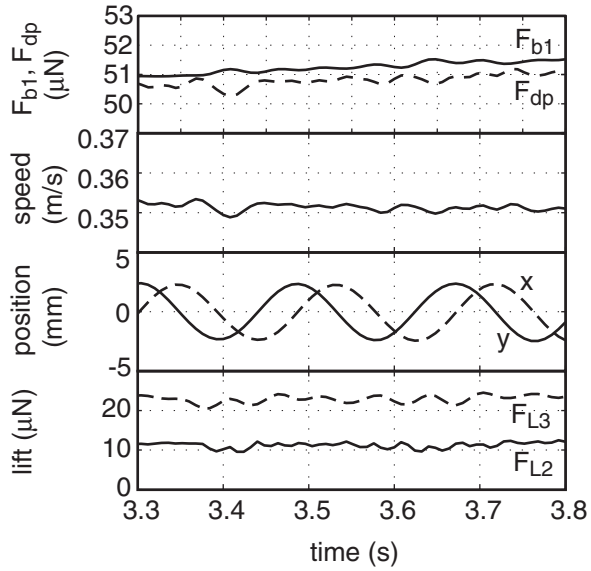

FIG. 14: The buoyancy component tangential to the path F_{b1}, potential flow drag F_{dp}, bubble velocity, horizontal position (x and y), and lift forces (solid line: F_{L2} and dashed line: F_{L3}) on the bubble during the spiral. The bubble radius is 1.12 mm at 1 atm. The measurement uncertainties are ± 0.5 μN for F_{b1} and F_{dp}, ± 7 mm/s for speed, $\pm$ 0.2 mm for position, and ± 4 μN for lift forces.

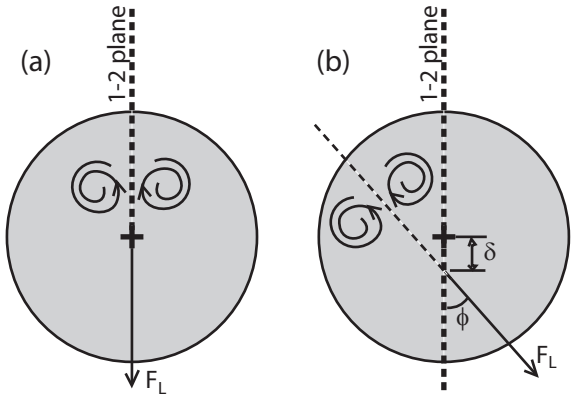

FIG. 16: Cartoon of a pair of wake vortices whose position is (a) symmetric about the 1-2 plane (zigzag) and (b) shifted away from the 1-2 plane as we hypothesize for the spiral.

B. Transition to spiral

In the following discussion we present a mechanism for the spiral state as well as the transition from zigzag to spiral. During the zigzag, the bubble motion is confined to a vertical plane (1-2 plane as defined above) and the two vortices in the wake of the bubble are symmetrically located on either side of that plane as illustrated in Fig. 16a. Since all the forces on the bubble are also confined to this plane, so is the bubble's path. Furthermore, the orientation of the 1-2 plane is constant in time. Recall that the transition to spiral motion occurs at a random time during the zigzag. Thus, let us examine a random perturbation which dislocates the wake vortices during the zigzag. In this situation, the wake vortices are shifted to one side so that the symmetry about the 1-2 plane is broken. Such a displacement has been reported in dye visualization studies by Lunde and Perkins [15]. As illustrated in Fig. 16b, we may quantify such a perturbation as a shift δ of the lift force with respect to the bubble center and an angle ϕ with respect to the 1-2 plane. A nonzero ϕ results in nonzero F_{L3} and hence a rotation of the 1-2 plane. F_{L3} typically reaches values about twice those of F_{L2}. The situation of a spiraling bubble corresponds to a particular value of $\phi = \phi_s$, which produces a rotation frequency of the 1-2 plane equal to the frequency of path oscillation. Indeed, if the 1-2 plane rotates by π radians during half a period of path oscillation, there is no longer a need for the wake reversal of the zigzag. The observation that this rotation of the 1-2 plane is necessary to explain why the wake of spiraling bubbles is smooth and continuous has been pointed out in wake visualization studies as well [5, 8]. For the bubble shown in Fig. 3, ϕ reaches a constant 0.3 radians during the spiral.

If $\phi < \phi_s$ just after a perturbation, then the rotation

rate of the 1-2 plane will not be large enough to generate a spiral. Instead the motion is similar to that during the transition from zigzag to spiral: a precessing ellipse. The 1-2 plane does not make a rotation of π radians before the wake reversal occurs. Now, in order for ϕ to grow, δ must be nonzero. In this case, the lift force does not act through the center of mass of the bubble. This results in a torque and hence a rotation of the wake vortices about the symmetry axis of the bubble, i.e. $d\phi/dt \neq 0$. We suppose that a nonzero δ is required initially to cause growth in the seed perturbation in ϕ eventually producing a spiral. More specifically, of all possible perturbations of the location of the wake vortices, only those with $\delta, \phi > 0$ or $\delta, \phi < 0$ are unstable. If δ and ϕ are of opposite sign then the rotation induced by δ will act to reverse the perturbation in ϕ, i.e. it is stable. Once an unstable perturbation occurs (as it inevitably will, given time), then the angle ϕ will grow through the course of the perturbed zigzag. When ϕ grows to a critical value, the wake rotation will be sufficient to maintain a stationary balance between buoyancy, acceleration, and lift; this is the spiral state.

Note that there is another possible mechanism that would result in a nonzero $d\phi/dt$. It is well known that two vortex lines of unequal strength will rotate about each other by mutual advection (e.g. [3]). This could provide the same torque as the offset δ in the above discussion. Although Schlieren visualization techniques suggest that the two vortices are quite similar in strength [8, 29], Brücker, using PIV measurements, suggests that one vortex may be stronger. Additional hydrodynamic measurements in the wake are needed to resolve this issue.

VII. CONCLUSIONS AND OPEN QUESTIONS

Several authors have previously pointed to vorticity production and transport as the underlying causes of the dynamics of millimeter sized rising bubbles [14, 15, 23]. From a complementary and consistent point of view, we describe physical mechanisms underlying the same dynamics based primarily on the geometry and structure of the bubble's path and wake. These descriptions are supported by precise experimental measurements of the full three dimensional trajectories of air bubbles rising through 2 meters of still water. From these measurements we deduce quantitative estimates of the forces acting on the bubbles.

We observe that for the rectilinear portion of bubble trajectories the measured drag matches Moore's prediction. The bifurcation to path instability is abrupt and perhaps subcritical. The bifurcated state always begins as a zigzag and evolves into a spiral. Qualitative and quantitative aspects of the path can be explained by the dynamics of a pair of streamwise vortices in the wake. The wake is responsible for lift forces on the bubble 10-40 μN in magnitude (buoyancy is typically 50-60 μN).

Several features of bubble path instability deserve further investigation. First, understanding of the onset to unstable path and wake would benefit from visualization, either numerical or experimental, of the flow very close to the rear of the bubble. Is the double-threaded vortex wake born out of an attached recirculating eddy? Second, such visualization data would also be useful in unravelling the causes of the transition from zigzag to spiral. Is one wake vortex stronger or, as we suggest, are the wake vortices simply unstable to rotation? Finally, we believe the frequency of path oscillation could be predicted using the torque balance in equations 5 and 9. In the same way that the balance between buoyancy and drag sets the terminal velocity of a straight rising bubble, the balance between the wake induced torque $\mathbf{\Gamma}_w$ and the drag $\mathbf{\Gamma}_d$ associated with rotation about the bubble's semimajor axis will determine the rotation rate of the bubble. This rotation rate is tied directly to the frequency of the path oscillations as was shown in section III. With expressions for $\mathbf{\Gamma}_w$ and $\mathbf{\Gamma}_d$ once could predict the path oscillation frequency. If the wake induced torque is unchanged in magnitude for zigzagging and spiraling bubbles, this would explain why the frequency of path oscillation is constant through the transition from zigzag to spiral.

VIII. ACKNOWLEDGEMENTS

The development of the ideas in this paper benefitted from many discussions at the Euromech colloquium 465, "Hydrodynamics of bubbly flows". In particular, we would like to thank Christian Veldhuis, Leen van Wijngaarden, Arie Biesheuvel, Andrea Prosperetti, Jacques Magnaudet, Frederic Risso, and Detlef Lohse. We also thank Arie Biesheuvel for permission to reprint the Schlieren photographs in Fig. 10. Finally, we appreciate the skilled work of Denis Le Tourneau and Pascal Metz in building the water tank and the ultrasound device respectively. This work was funded by École Normale Supérieur, Centre National de la Recherche Scientifique, and Region Rhone-Alpes, Emergen.

[1] N. M. Aybers and A. Tapucu, "The motion of gas bubbles rising through stagnant liquid," Wärme- und Stoffübertragung **2**, 118 (1969).

[2] N. M. Aybers and A. Tapucu, "Studies on the drag and shape of gas bubbles rising through stagnant liquid," Wärme- und Stoffübertragung **2**, 171 (1969).

[3] Batchelor, G. K., *An introduction to fluid dynamics* (Cambridge University Press, Cambridge, 1967).

[4] T. B. Benjamin, "Hamiltonian theory for motions of bubbles in an infinite liquid," J. Fluid Mech. **181**, 349 (1984).

[5] C. Brücker, "Structure and dynamics of the wake of bub-

bles and its relevance for bubble interaction," Phys. Fluids **11**, 1781 (1999).
[6] R. Clift, J. R. Grace, and M. E. Weber, "*Bubbles, Drops, and Particles* (Academic, New York, 1978).
[7] A. W. G. de Vries, "Path and wake of a rising bubble," (PhD dissertation, University of Twente, Netherlands, 2001).
[8] A. W. G. de Vries, A. Biesheuvel, and L. van Wijngaarden, "Notes on the path and wake of a gass bubble rising in pure water," Int. J. Multiphase Flow **28**, 1823 (2002).
[9] P. C. Duineveld, "The rise velocity and shape of bubbles in pure water at high Reynolds number," J. Fluid Mech. **292**, 325 (1995).
[10] K. Ellingsen and F. Risso, "On the rise of an ellipsoidal bubble in water: oscillatory paths and liquid-induced velocity," J. Fluid Mech. **440**, 235 (2001).
[11] R. A. Hartunian and W. R. Sears, "On the instability of small gas bubbles moving uniformly in various liquids," J. Fluid Mech. **3**, 27 (1957).
[12] M. S. Howe, "On the force and moment on a body in an incompressible fluid, with application to rigid bodies and bubbles at low and high Reynolds numbers", Q. J. Mech. Appl. Math. **48**, 401 (1995).
[13] H. Lamb, *Hydrodynamics, 6th ed.* (Dover Publications, New York, 1945).
[14] L. G. Leal, "Vorticity transport and wake structure for bluff bodies at finite Reynolds number," Phys. Fluids A **1**, 124 (1989).
[15] K. Lunde and R. J. Perkins, "Observations on wakes behind speroidal bubbles and particles," Paper No. FEDSM'97-3530, 1997 ASMEFED Summer Meeting, Vancouver, Canada, page 1.
[16] J. Magnaudet and I. Eames, "The motion of high-Reynolds-number bubbles in inhomogeneous flows," Ann. Rev. Fluid Mech. **32**, 659 (2000).
[17] J. Mercier, A. Lyrio, and R. Forslund, "Three dimensional study of the nonrectilinear trajectory of air bubbles rising in water," J. App. Mech. **40**, 650 (1973).
[18] D. W. Moore, "The velocity of rise of distorted gas bubbles in a liquid of small viscosity," J. Fluid Mech. **23**, 749 (1965).
[19] N. Mordant, J.-F. Pinton, and O. Michel, "Time-resolved tracking of a sound scatterer in a complex flow: Nonstationary signal analysis and applications," J. Acoust. Soc. Am. **112**, 108 (2002).
[20] N. Mordant and J.-F. Pinton, "Velocity measurements of a settling sphere," Eur. Phys. J. B **18**, 343 (2000).
[21] N. Mordant, P. Metz, O. Michel, and J.-F. Pinton, "An acoustic technique for Lagrangian velocity measurements," Rev. Sci. Instr. **76**, 025105 (2005).
[22] G. Mougin and J. Magnaudet, "The generalized Kirchhoff equations and their application to the interaction between a rigid body and an arbitrary time-dependent viscous flow", Int. J. Mulitphase Flow **28**, 1837 (2002).
[23] G. Mougin and J. Magnaudet, "Path instability of a rising bubble." Phys. Rev. Lett. **88**, 014502 (2002).
[24] G. Mougin, "Interactions entre la dynamique d'une bulle et les instabilitiés de son sillage," (PhD Dissertation, Institute National Polytechnique de Toulouse, France, 2002).
[25] C. D. Ohl, A. Tijink and A. Prosperetti, "The added mass of an expanding bubble," J. Fluid Mech. **482**, 271 (2003).
[26] A. Prosperetti, "Bubbles," *Phys. Fluids* **16**, 1852 (2004).
[27] P. G. Saffman, "On the rise of small air bubbles in water," J. Fluid Mech. **1**, 249 (1956).
[28] H. Sakamoto and H. Hanui, "The formation mechanism and shedding frequency of vortices from a sphere in uniform shear flow," J. Fluid Mech. **287**, 151 (1995).
[29] C. Veldhuis, Personal communications, 2005.
[30] M. Wu and M. Gharib, "Experimental studies on the shape and path of small air bubbles rising in clean water," Phys. Fluids **14**, L49 (2002).